HHS Public Access

Author manuscript

J Magn Reson Imaging. Author manuscript; available in PMC 2018 October 07.

Published in final edited form as:

J Magn Reson Imaging. 2018 October ; 48(4): 938–950. doi:10.1002/jmri.25963.

Characterization of Active and Infiltrative Tumorous Subregions From Normal Tissue in Brain Gliomas Using Multiparametric MRI

Anahita Fathi Kazerooni, PhD[1,2], **Mahnaz Nabil, PhD**[3], **Mehdi Zeinali Zadeh, MD**[4], **Kavous Firouznia, MD**[5], **Farid Azmoudeh-Ardalan, MD**[6], **Alejandro F. Frangi, PhD**[7], **Christos Davatzikos, PhD**[8], and **Hamidreza Saligheh Rad, PhD**[1,2,*]

[1]Quantitative MR Imaging and Spectroscopy Group, Research Center for Molecular and Cellular Imaging, Tehran University of Medical Sciences, Tehran, Iran

[2]Department of Medical Physics and Biomedical Engineering, Tehran University of Medical Sciences, Tehran, Iran

[3]Department of Statistics, Faculty of Mathematical Science, University of Guilan, Rasht, Iran

[4]Department of Neurological Surgery, Imam Khomeini Hospital, Tehran University of Medical Sciences, Tehran, Iran

[5]Advanced Diagnostic and Interventional Radiology Research Center, Imam Khomeini Hospital, Tehran University of Medical Sciences, Tehran, Iran

[6]Department of Pathology, Imam Khomeini Hospital, Tehran University of Medical Sciences, Tehran, Iran

[7]Department of Electronic and Electrical Engineering, University of Sheffield, Sheffield, UK

[8]Department of Radiology, University of Pennsylvania, Philadelphia, Pennsylvania, USA

Abstract

Background—Targeted localized biopsies and treatments for diffuse gliomas rely on accurate identification of tissue subregions, for which current MRI techniques lack specificity.

Purpose—To explore the complementary and competitive roles of a variety of conventional and quantitative MRI methods for distinguishing subregions of brain gliomas.

Study Type—Prospective.

Population—Fifty-one tissue specimens were collected using image-guided localized biopsy surgery from 10 patients with newly diagnosed gliomas.

Field Strength/Sequence—Conventional and quantitative MR images consisting of pre- and postcontrast T_1w, T_2w, T_2-FLAIR, T_2-relaxometry, DWI, DTI, IVIM, and DSC-MRI were acquired preoperatively at 3T.

Assessment—Biopsy specimens were histopathologically attributed to glioma tissue subregion categories of active tumor (AT), infiltrative edema (IE), and normal tissue (NT) subregions. For

*Address reprint requests to: H.S.R., Kaboli Building, Imam Khomeini Hospital, Keshavarz Blvd., Tehran, Iran. h-salighehrad@tums.ac.ir.

each tissue sample, a feature vector comprising 15 MRI-based parameters was derived from preoperative images and assessed by a machine learning algorithm to determine the best multiparametric feature combination for characterizing the tissue subregions.

Statistical Tests—For discrimination of AT, IE, and NT subregions, a one-way analysis of variance (ANOVA) test and for pairwise tissue subregion differentiation, Tukey honest significant difference, and Games-Howell tests were applied ($P < 0.05$). Cross-validated feature selection and classification methods were implemented for identification of accurate multiparametric MRI parameter combination.

Results—After exclusion of 17 tissue specimens, 34 samples (AT = 6, IE = 20, and NT = 8) were considered for analysis. Highest accuracies and statistically significant differences for discrimination of IE from NT and AT from NT were observed for diffusion-based parameters (AUCs >90%), and the perfusion-derived parameter as the most accurate feature in distinguishing IE from AT. A combination of "CBV, MD, T_2_ISO, FLAIR" parameters showed high diagnostic performance for identification of the three subregions (AUC ~90%).

Data Conclusion—Integration of a few quantitative along with conventional MRI parameters may provide a potential multiparametric imaging biomarker for predicting the histopathologically proven glioma tissue subregions.

Level of Evidence—2

Technical Efficacy—Stage 3

Diffuse gliomas manifest extensive diffuse infiltration of tumor cells in adjacent brain parenchyma.[1] Even when low grade, diffuse gliomas are generally fatal after several years.[1,2] It is widely known that characteristic spatial intratumor variability within the microenvironment of gliomas account for the grim prognosis of these patients.[3,4] Within heterogeneous tumors like gliomas, multiple subregions with different phenotypic characteristics coexist, which often represent heterogeneous genetic and microenvironmental profiles, likely to respond variably to treatment.[5,6] Lack of sensitive and specific quantitative imaging biomarkers for realizing spatial variations of gliomas and localizing the most aggressive portion of the tumor leads to inaccurate biopsy sampling, which hinders target-specific diagnosis and therapies.[5]

Targeted biopsy procedures and surgical/treatment planning for gliomas most often rely on conventional contrast-enhanced T_1-weighted (CE-T_1w), T_2-weighted (T_2w) and T_2-FLAIR images.[7–9] Nonetheless, as diffuse gliomas tend to invade the brain tissue in small cell groups, tumor expansion and progression may precede changes in contrast enhancement.[1,8] Furthermore, CE-T_1w cannot sufficiently localize the most aggressive or active tumor subcompartment to ensure reliable biopsy outcome.[10,11] On the other hand, T_2w hyperintense regions are incapable of characterizing the infiltrative glioma subregion (infiltrative edema, also referred to as nonenhancing tumor [NET]), and diffuse infiltrating cells can be found beyond the extent of T_2w hyperintensity borders.[12,13] Hence, based on conventional magnetic resonance imaging (MRI), stratification of the most aggressive/active part of the tumor and infiltrative glioma and detection of the extent of invasion from normal tissue remains challenging.

Various advanced MRI contrasts have been explored for their potential in localizing and grading glioma brain tumors. Diffusion-weighted imaging (DWI) and diffusion tensor imaging (DTI) reflect the water proton mobility related to changes in cellular density, permeability of the cell membrane, and tissue microstructure.[14,15] Perfusion-weighted imaging (PWI) visualizes microvascular changes and cellular proliferation; particularly, regional cerebral blood volume (rCBV) derived from dynamic susceptibility contrast-enhanced (DSC)-MRI correlates with the degree of neovascularization and histopathological grade, surpassing the performance of CE-T_1w MRI.[16–18]

There have been sporadic attempts to study the role of quantitative MRI methods, including DSC-MRI, DWI/DTI, IVIM, and T_2-relaxometry for characterizing infiltrating glioma regions through biopsy validation.[18–20] Hence, we sought to address: 1) the roles of individual MRI-derived parameters in differentiation of the three subregions, ie, active tumor (AT), infiltrative edema (IE), and normal tissue (NT), from each other; 2) the relationship between MRI-derived parameters with histopathological cellular density; and 3) the best multiparametric combination of MRI-derived features for discrimination of AT, IE, and NT through a quantitative methodology.

Materials and Methods

Patients

Between July 2015 and February 2016, 10 adult patients (six men and four women; mean age 40.4 years; age range, 20-76 years) with newly diagnosed gliomas were prospectively recruited for this study. The patients underwent presurgical MRI and computed tomography (CT) examinations, followed by image-guided neurosurgery within 1-3 days from image acquisition. Institutional Review Board (IRB) approval was obtained and the patients provided informed written consent to be included in the study, designed in compliance with the Health Insurance Portability and Accountability Act (HIPAA) law. Inclusion criteria for this study consisted of patients: 1) with suspected glioma brain tumors based on their initial MR scan; 2) with no prior treatment, including surgery or radiotherapy; 3) having no contraindications for surgery; 4) in whom the tumor was not in an eloquent area; and 5) for whom there were no technical challenges for performing surgery.

Patients or biopsy specimens were excluded if 1) they did not undergo surgery; 2) imaging was performed inadequately or some image sequences were missing; or 3) if histopathological assessment of gross tumor or specimens was impossible or not provided.

Image Acquisition

All patients underwent preoperative MRI acquisition within 2 days prior to their surgery. Structural and physiological MRI acquisitions were performed on a 3T MRI scanner (Siemens Magnetom Tim Trio, Erlangen, Germany). Sagittal T_2w turbo spin echo (repetition time/echo time [TE/TR] = 80/6000, slice thickness = 5 mm, flip angle = 140°, field of view [FOV] = 230 × 230 mm^2, image matrix = 320 × 320, pixel size = 0.72 × 0.72 mm^2). Axial T_2w turbo spin echo (TE/TR = 106/5400, slice thickness = 5 mm, flip angle = 120°, FOV = 200 × 200 mm^2, image matrix = 232 × 256, pixel size = 0.78 × 0.78 mm^2). Axial fluid

attenuated inversion recovery (FLAIR) (TE/TR/TI = 115/8400/2240, slice thickness = 5 mm, flip angle = 125°, FOV = 181 × 200 mm^2, image matrix = 232 × 256, pixel size = 0.78 × 0.78 mm^2). Axial 3D magnetization-prepared rapid-acquisition gradient-echo (MP-RAGE) T_2w spin-echo as a part of image-guided surgery protocol with TE/TR = 200/2500, slice thickness = 1mm, flip angle = 120°, FOV = 208 × 256 mm^2, image matrix = 420 × 512, pixel size = 0.50 × 0.50 mm^2.

Axial DWI using echo-planar imaging (EPI) sequence with TE/TR = 100/4000, slice thickness = 5 mm, flip angle = 90°, FOV = 200 × 200 mm^2, image matrix = 136 × 136, pixel size = 1.47 × 1.47 mm, b-value = 50, 1000 s/mm^2. Axial multi b-value DWI using EPI method with TE/TR = 100/4000, slice thickness = 5 mm, flip angle = 90°, FOV = 200 × 200 mm^2, image matrix = 136 × 136, pixel size = 1.47 × 1.47 mm^2, b-values = 0, 50, 200, 400, 600, 800, 1000 s/mm^2. Diffusion tensor imaging (DTI) with 64 directions and TE/TR = 90/9000, slice thickness = 5 mm, FOV = 256 × 256 mm^2, flip angle = 90°, number of excitations (NEX) = 1, image matrix = 128 × 128 × 72, pixel size = 1.72 × 1.72 mm^2, b-value = 50, 1000 s/mm^2.

Axial multiecho T_2w spin-echo (T_2-relaxometry) was carried out with TR = 4000 msec, TE = 12, 24, 36, 48, 60, 72, 84, 96, 108, 120, 132, 144, 156, 168, 180, 192 msec, slice thickness = 5 mm, flip angle = 180°, FOV = 200 × 200 mm^2, image matrix = 232 × 256, pixel size= 0.78 × 0.78 mm^2.

After injection of 0.2 mmol/kg of Gadovist (Bayer Schering Pharma, Berlin, Germany) at a rate of 5 ml/s and followed by a 20-mL saline flush, DSC-MRI was acquired using a GE-EPI sequence with TE/TR = 30/1600, slice thickness = 5 mm, FOV = 220 × 220 mm^2, flip angle = 70°, NEX = 1, image matrix = 128 × 128 × 20, pixel size = 1.72 × 1.72 mm^2, number of dynamic scans = 64, temporal resolution = 1.5 sec. To minimize the effects of contrast agent extravasation a preload of contrast agent was administered with about 25% of the total contrast dose about 4 minutes of incubation time before the second injection for DSC-MR imaging.

Pre- and postcontrast axial 3D MP-RAGE T_1w spin-echo were also acquired as a part of the protocol required for the navigation system TE/TR = 5/17, slice thickness = 1 mm, flip angle = 25°, FOV = 208 × 256 mm^2, image matrix = 208 × 256, pixel size = 1 × 1 mm^2.

MRI pulse sequences and their parameter adjustments are summarized in Table 1.

CT images were acquired for all patients prior to surgery to ensure accurate registration of the images with the position of the patient during image-guided neurosurgery. 3D images were acquired on a 64-slice CT scanner (GE Healthcare Technologies, Milwaukee, WI) with no gantry tilt, slice thickness of 0.625 mm, from maxilla to the top of the head.

Quantification of MR Images

DTI—Quantification of DTI was executed in ExploreDTI software (v, 4.8.6)[21] with proper parameter adjustments, and after EPI and patient motion correction. Maps of mean diffusivity (MD), fractional anisotropy (FA), and L1, L2, and L3 eigenvalues were exported

from the software. Pure isotropic diffusion and pure anisotropic diffusion maps denoted by P and Q, respectively, were calculated based on this formula[22]:

$$P = \sqrt{3}MD = \frac{\lambda_1 + \lambda_2 + \lambda_3}{\sqrt{3}}$$

$$Q = \sqrt{(\lambda_1 - MD)^2 + (\lambda_2 - MD)^2 + (\lambda_3 - MD)^2}$$

DSC-MRI—DSC-MRI analysis was carried out based on an algorithm developed in-house, which inputs signal intensity–time curves of T_2^*-based dynamic images in each pixel, converts them to ΔR_2^* curves, selects the arterial input function (AIF) based on a modified automated algorithm, performs decorrelation using block-circulant SVD, and generates a regional CBV (rCBV) map.

T_2/PROTON DENSITY MAPPING—In T_2-relaxometry, images are acquired at multiple echo times to obtain an estimate of T_2 and proton density by fitting the following equation to the signal:

$$S = S_0 e^{-\frac{TE}{T_2}}$$

where S_0 is the proton density and T_2 is the spin–spin relaxation. Quantitative T_2 and proton density (PD) maps were generated by pixelwise fitting of the mentioned equation to the corresponding multiecho signal.

QUANTIFICATION OF INTRAVOXEL INCOHERENT MOTION—Diffusion-weighted images are highly affected by flow of blood and cerebrospinal fluids at very low b-values (ie, less than 100–200 s/mm^2).[23,24] Here, to separate contributions of diffusion and perfusion, the bi-exponential intravoxel incoherent motion (IVIM) model is used which is denoted by[24]:

$$S = S_0\left(fe^{-bD*} + (1-f)e^{-bD}\right)$$

where S_0 is the signal at b-value of zero, f is the fraction of signal affected by flow, D* describes the decay of signal caused by flow, and D is the measured diffusion coefficient, which is a function of diffusion time. To nullify the effect of flow on diffusion measurements, diffusion coefficients (D) for each voxel were calculated using conservative minimum b-values of 200 s/mm^2.[25] As diffusion parameters are highly affected by non-Gaussian behavior of diffusion at higher b-values, for calculation of D, this effect was conservatively cancelled by using maximum value of 600 s/mm^2.

To account for non-Gaussianity of the signal in higher *b*-values, the modified IVIM model including diffusion kurtosis imaging (IVIM-DKI) was considered[26]:

$$S = S_0\left(fe^{-bD*} + (1-f)e^{-bD+\frac{b^2D^2K}{6}}\right)$$

where K is the kurtosis factor that measures deviation from the Gaussian behavior. D for each voxel was estimated by fitting the equation to the segment of the signal at *b*-values of 200, 400, and 600 s/mm^2, and K was estimated from b-values of 600, 800, and 1000 s/mm^2 using nonlinear least-squares method.

Biopsy Site Selection

The generated maps from different modalities, including rCBV-map from DSC-MRI, ADC-map from DWI, maps of FA, MD, P, Q from DTI, maps of D, D*, f, and K from multi-b-value diffusion imaging, maps of T_2 and PD from T_2-relaxometry technique, and conventional images comprising of FLAIR, T_2_ISO (MP-RAGE T_2w), and MP-RAGE precontrast T_1w, were coregistered with the postcontrast MP-RAGE T_1w (CE-T_1w) image using a rigid registration method with normalized mutual information (NMI) as the similarity measure in SPM software (http://www.fil.ion.ucl.ac.uk/spm/). The difference between post- and precontrast T_1w images was calculated to form T_1_SUB (subtracted T_1w) image, which shows the enhanced regions (Fig. 1).

A senior radiologist (K.F. with 12 years of experience in neuroradiology) identified the biopsy targets, ie, active tumor, infiltration, and normal regions, based on the presence of hyperintensity on CE-T_1w, hypointensity on T_2w and FLAIR images, and according to quantitative ADC and rCBV maps. Rectangular regions of interest (ROIs) with sizes of at most 8 × 8 pixels were marked on CE-T_1w images and imported into the navigation workstation to plan for image-guided biopsy intervention. The regions were ideally identified on areas with best accessibility for the neurosurgeon for specimen collection and distant from vessels, ventricles, and critical brain regions.

Image-Guided Tissue Biopsy Procedure

The specimens were sampled from the patients by a senior neurosurgeon (M.Z. with 10 years of experience in neurosurgery) using a disposable biopsy needle (Stryker, Switzerland). The coordinates of the ROIs were recorded by the navigation system (OpticVision, Parseh Intelligent Surgical Systems [PARSISS], Iran), which were used to overlay on the images and MRI-derived quantitative maps. Based on the guide provided by navigation, needle biopsy was performed on all target points. For each patient, 4–6 specimens with at least 1-cm of distance were collected for histopathological assessments.

These technical considerations were addressed during the biopsy to minimize intraoperative brain shift and error:

1. The target points were presurgically marked in the order of normal tissue, edema, tumor, and necrosis;
2. Serum manitol, corticosteroids, or any other diuretics pre/intraoperative were not given to patients prior to biopsy procedure;
3. Hypo/hyperventilation during surgery was avoided;
4. Minimal dural opening was performed to prevent CSF egress resulting in brain shift;
5. The target points in proximity of the ventricles were the last points for biopsy, to avoid unwanted entrance into the ventricles, resulting in CSF drainage and therefore changing navigation accuracy due to brain shift;
6. For the target points in proximity of cystic portions within the tumor, a similar strategy was adopted.

After needle biopsy, the dura was opened and based on preoperative images, complete resection of the tumor was performed and the resected gross tumor volume was transferred for histopathological grading.

Histopathological Assessment of Tissue Samples

After being removed from the brain, the specimens were fixed in 10% buffered formalin and routinely processed for histopathological assessment. Five micrometer sections were stained using the hematoxylin and eosin (H&E) method and reviewed by a pathologist (F.A. with 20 years of experience in neuropathology). For each specimen, the pathologist determined the presence of tumor cells and scored the samples as “normal tissue” where no tumor cells were identified, “positive tumor cells” when infiltrating tumor cells were present, and “tumor core” when tumor constituted the majority of tissue. Tumor was identified, classified, and graded based on morphological features, such as density and distribution of cells, nuclear atypia, mitotic activity, vascular proliferation, and necrosis. Throughout this article we refer to the pathological term “tumor core” as “active tumor (AT),” “positive tumor cells” as “infiltrating edema (IE),” and “normal tissue” as “normal tissue (NT).”

For each specimen, the area with the highest cellularity was selected and one image was captured at ×40 magnification. Quantitative assessment of histology images was performed automatically by a cell segmentation method which applies decorrelation and stretching of the colorspace in the preprocessing step for improving the performance of cell segmentation (Fig. 2).[27] Cellular count (CC) within the specified area was calculated from the segmented images and used as a representative parameter of cellular density. The relationship between the calculated CC on all regions and interpretation of the pathologist, as the gold standard, was examined.

Statistical Analysis

The statistical analysis comprised of the following steps: 1) evaluating the association of MRI-derived parameters with each other and with statistically significant quantitative histopathological feature (cellular count); 2) assessing mean values of the extracted features

among the three tissue subtypes, ie, IE, NT, and AT; 3) investigating the diagnostic performances of individual MRI-derived features for distinguishing the histopathologically identified regions and their combinations based on a machine-learning technique, including automatic feature selection and classification procedures.

The computed MRI-based features ($n = 15$) include morphological parameters, ie, T_1_SUB, T_2_ISO, FLAIR, diffusion-related parameters, ie, ADC, MD, FA, P, Q, D, D*, K, perfusion-related parameters, ie, CBV, and f, and T_2-relaxometry parameters, ie, T_2 and PD. The histopathological CC metric was also evaluated for its potential in discriminating the subregions. All statistical analysis and machine-learning procedures were performed in R Statistical Software (R3.0.2, Vienna, Austria).

COMPARISON OF MEAN VALUES—The one-way analysis of variance (ANOVA) method was applied to evaluate the discrimination of NT, IE, and AT tissue subtypes based on the MRI-derived parameters and cellular count. $P < 0.05$ was considered significant for differentiation of the three tissue regions simultaneously. For each parameter, pairwise differentiation of the regions, namely, NT from IE, NT from AT, and IE from AT, was assessed by post-hoc tests: Tukey's honest significant difference (Tukey-HSD) or Games-Howell methods, to avoid Type I errors by adjusting the calculated *P*-values for multiple comparisons. The HSD test is based on assumptions of normality and equality of variance; the former was evaluated using normality tests and the latter by the Bartlett method. If equality of variance assumption passed, Tukey-HSD was performed; otherwise, Games-Howell nonparametric test was applied.

ASSOCIATION OF PARAMETERS—Relationships between MRI-derived parameters with each other and also between them and cellular count were obtained using Spearman's rank correlation. To correct for multiple comparisons, Holm's method for multiple testing[28] was applied and, after correction, a level of 0.05 was considered statistically significant.

ASSESSMENT OF DIAGNOSTIC PERFORMANCES OF INDIVIDUAL MRI-DERIVED PARAMETERS—Fischer's linear discriminant analysis (LDA) method was used to assess performances of MRI-derived and CC parameters in discrimination of NT from IE, NT from AT, and IE from AT. LDA was implemented with leave-one-out crossvalidation (LOOCV), where in each iteration (number of iterations equals the number of samples), the dataset is partitioned into the training set composed of whole data excluding one sample, which is separated as the test object. Assessment metrics, namely sensitivity, specificity, accuracy, and area under the receiver operating characteristic (ROC) curve (AUC) were calculated on test samples and averaged over loops of crossvalidation.

COMBINATION OF MRI-DERIVED PARAMETERS THROUGH CLASSIFICATION—To identify the complementary/competitive roles of MRI-derived features, feature selection was carried out using Akaike Information Criterion (AIC)[29] and Schwarz Bayesian Information Criterion (BIC)[30] in forward selection, backward elimination, and stepwise selection strategies (constructing six feature selection methods) on a feature space consisting of the 15 MRI-derived parameters.

The feature selection algorithm was adjusted to avoid choosing similar parameters in a set, eg, the algorithm should select only one feature among diffusion-related features: ADC, D, MD, P; anisotropy-related features: FA, Q; perfusion-related features: f, CBV; T_2-related features: T_2, T_2_ISO.

Feature selection was performed in loops of LOOCV and the most frequently selected feature subsets by each of the feature selection methods were the representative feature subset.[31] This was followed by a classification step based on Fischer's linear discriminant analysis (LDA), quadratic discriminant analysis (QDA), and support vector machine (SVM) methods[32] for discrimination of tissue subtypes. To avoid bias, classification was also performed using LOOCV.

Results

Among the 10 recruited patients, six were diagnosed with low-grade glioma (WHO Grade II: low-grade astrocytoma [$n = 3$], diffuse oligoastrocytoma [$n = 2$], oligodendroglioma [$n = 1$]), one with anaplastic oligoastrocytoma (WHO Grade III), and three with glioblastoma multiforme (WHO Grade IV). A total of 51 tissue specimens were collected from 10 patients. Three patients (two GBM and one Grade II oligodendroglioma) were excluded due to the absence or distorted multi-b-value, multiecho, DTI, or DSC-MRI. Finally, seven patients with 34 samples were included in the study. Based on qualitative histopathological assessment, six samples were diagnosed as the "tumoral core," 20 samples as "positive tumor cells," and 8 samples as "normal tissue."

Relationship of MRI Parameters

The summary results for correlations among the MRI parameters with each other and with CC are provided in Table 2. The statistically significant correlations are shown in boldface type and are shaded in gray.

DIFFUSION-BASED PARAMETERS—ADC parameter significantly correlated with MD, P, D, T_2_ISO, and T_2 and negatively with FA and K. This parameter showed the strongest correlations with D (R = 0.96), MD (R = 0.91), P (R = 0.88), and T_2 (R = 0.80), but showed no significant correlation with CC.

D is directly correlated with ADC, FA, MD, P, T_2_ISO, T_2, and inversely correlated with K. The strongest correlation of D was with ADC (R = 0.96), MD (R = 0.90), and P (R = 0.88). It showed significant correlation with CC (R = 0.40).

D* was correlated poorly and inversely with T_2. K correlated inversely with ADC, MD, P, and T_2 (in all, $R \leq 0.62$). Besides the correlations mentioned earlier that included MD, this parameter was strongly correlated with P (R = 0.98) and T_2 (R = 0.84), and showed moderate correlations with T_2_ISO. P was highly related to T_2 (R = 0.81), and moderately correlated with T_2_ISO. Both MD and P were correlated with CC (R = 0.36).

FA was strongly correlated with Q (R = 0.86) and indicated a modest inverse association with ADC, D, MD, P, and T_2. Furthermore, FA showed an inverse correlation with CC (R = −0.37). Q was directly correlated with FA, and showed no relationships with CC.

PERFUSION-BASED PARAMETERS—CBV only showed statistically significant correlation with the f parameter derived from IVIM, which was not strong (R = 0.35). Additionally, it indicated a significant correlation with CC (R = 0.46). Parameter f correlated with none of the parameters except CBV.

CMRI PARAMETERS—FLAIR only correlated with T_2_ISO with a correlation coefficient of 0.67. T_2_ISO was significantly associated with ADC, D, MD, FA, FLAIR, and P (for all, R <0.70). T_1_SUB showed no significant correlations with any of the parameters.

T_2-MAPPING PARAMETERS—As mentioned in previous sections, T_2 demonstrated correlations with ADC, D, K, MD, P, and T_2_ISO. The PD-map correlated with none of the parameters.

Association of Tissue Subtypes With Quantitative MRI-Derived Parameters

Comparison of the mean values of individual parameters based on the ANOVA test for differentiation of the three tissue subtypes from each other is shown in Table 3. The results suggest that among MRI-derived parameters, T_2_ISO, FLAIR, ADC, CBV, MD, FA, P, D, and T_2 show statistically significant differences among the three subregions, ie, NT, IE, and AT. The histopathologically derived parameter, CC, showed statistically significant differences among the three tissue subregions (P = 8.9E-06).

The details of classification performances of individual parameters in differentiation of each of the two subregions from each other and based on the crossvalidated LDA method are given in Table 3. For differentiation of NT from IE (requiring high sensitivity), the highest performances were for T_2_ISO, FLAIR, ADC, MD, P, D, and T_2. T_2-based features, ie, T_2_ISO, FLAIR, and T_2 resulted in AUCs >84% for this discrimination. The four diffusion-related parameters, ie, ADC, MD, P, and D, resulted in AUCs of over 90% (and sensitivities >90%) for discrimination of NT from IE. In this context, T_1_SUB, CBV, and f were highly sensitive (100%) but lacked specificity.

All MRI-derived parameters except for D*, f, and PD were accurate for separation of NT from AT, implying high sensitivity of these metrics.

The only statistically significant MRI-derived feature for identification of IE from AT was DSC-MRI-derived parameter, ie, CBV, with high specificity of 95%.

CC showed high AUCs for differentiation of the three two-by-two subregions (>84%), although its specificity for separation of NT from IE was rather low.

Combination of Quantitative MRI-Derived Parameters

For classification of the three tissue subtypes from each other, ie, NT, IE, and AT, four feature combinations were selected by the feature selection methods: 1) CBV, MD, FLAIR,

T_2_ISO (selected by backward AIC); 2) CBV, MD (selected by backward BIC); 3) CBV, D, T_2_ISO (forward/stepwise AIC); and 4) CBV, D (selected by backward BIC) (Table 4). Three classification methods, namely, LDA, QDA, and SVM, were applied on the selected combinations. As Table 4 summarizes, using the classifiers the most accurate feature set was "CBV, MD, FLAIR, T_2_ISO" with AUC of ~90% for all three classifiers. Additionally, the feature combination "CBV, D, T_2_ISO" resulted in AUC of ~92% using the LDA classification scheme.

Table 5 shows the performances of classification schemes (each classifier on the selected feature subsets) for two-by-two discrimination of the three subregions from each other. The combination of "CBV, MD, FLAIR, T_2_ISO" using either QDA or SVM classifiers produces accurate results for all three discrimination purposes, ie, NT from IE, NT from AT, and IE from AT. Using QDA, this combination indicates an AUC of 92.3% for characterization of NT from IE, 100% for NT from AT, and 89.2% for IE from AT. SVM classification based on this combination results in AUC of 98.8% for identification of NT from IE, 100% for NT from AT, and 100% for IE from AT.

Additionally, "CBV, D, T_2_ISO" using the QDA classifier can generate AUC of 85.6% for differentiation of NT from IE, 100% for NT from AT, and 91.6% for IE from AT.

Discussion

Conventional MRI lacks accuracy in assessing physiological variations and regional heterogeneity within tumors. During the past years, several quantitative methods, such as DWI/DTI and DSC-MRI, have been investigated for their potential as adjuncts to conventional MRI. Yet the comparative and complementary roles of these methods and emerging techniques, such as T_2-relaxometry and IVIM, are not explored, especially through histopathologically proven specimens and objective classification techniques.

In this preliminary study, we attempted to tackle this problem by evaluation of the aforementioned techniques on localized biopsy specimens, which were histopathologically assessed and attributed to AT, IE, and NT subregions. Among individual MRI-derived parameters, diffusion-related ADC, MD, P, D parameters, as markers of cellular proliferation, indicated high classification performance for identification of NT from IE, and NT from AT, but were not suitable for IE from AT separation. This finding along with significant correlation of D, MD, and P with histopathological CC parameter suggests that changes in cellular distribution captured by diffusion-based parameters can be early markers of glioma infiltration (NT from IE discrimination). But these changes in low-grade glioma are not significantly different among IE and AT subregions; therefore, these parameters may not be diagnostically valuable for localizing the most active part of the tumor and other features must be explored. Among FA and Q as indicators of diffusion anisotropy, FA was statistically significant for discrimination of the three subregions and showed significant inverse correlation with CC, and accurately discriminated NT from AT. However, FA did not result in statistically significant differences for isolation of NT from IE or IE from AT in our sample population.

In animal studies, DTI has been shown to identify microinfiltration of tumor cells in the surrounding brain tis- sue.[33,34] Early investigations on human brain glioma indicate that DWI/DTI can provide helpful information for assessment of peritumoral edema and to define margins of tumor invasion.[3,35,36] Specifically, ADC[20,37] or MD and FA[19,38,39] have shown correlations with NET based on histopathologically proven biopsy specimens.

Unlike other MRI-derived parameters, CBV was the only statistically significant feature for discrimination of IE from AT. Hence, early vascularization is a discriminative factor for identifying the most active component of gliomas. This parameter was not statistically significant for identification of NT from IE, indicating that in the early stages of infiltration and before transforming into the most active subpopulations, neoangiogenesis may not have a role in gliomas. CBV was evidently statistically significant for characterization of NT from AT. Nonetheless, the classification performance was lower than that of diffusion-based parameters. The suboptimal performance of CBV in contrast to diffusion-based parameters in this context can be attributed to our sample population of low-grade gliomas, in which neovascularization has not become largely prominent in the infiltrative or active tumor regions.

The best combination of these parameters was sought using crossvalidated feature selection and classification methods. Three classifiers with increasing complexity, namely, LDA, QDA, and SVM, were implemented to obtain insights about the capability of the selected feature combinations in tissue identification irrespective of classifier formulation. In all four selected feature sets, CBV and a diffusion- based parameter like D or MD were present, signifying the importance of perfusion and diffusion parameters in subregion characterization. Incorporation of T_2_ISO and FLAIR to perfusion and diffusion parameters in the form of the “CBV, MD, T_2_ISO, and FLAIR” combination resulted in high classification performance for characterization of the three tissue subregions from each other, using the classifiers (AUC ~90%). This feature set revealed high classification performance in pairwise subregion classification as well. T_2_ISO and FLAIR are important factors for illustrating the pathogenic changes within glioma borders. Similar integration of parameters has been intuitively employed in brain tumor segmentation elsewhere.[40–42]

A combination of fewer parameters including “CBV, D, T_2_ISO” based on the QDA classifier generated a relatively high classification performance for pairwise differentiation of tissue subregions. For occasions with high risk of patient discomfort and motion, IVIM acquisition combined with DSC-MRI perfusion and anatomical high-resolution T_2w, required for image-guided neurosurgery, could be performed without addition of DTI acquisition, which is highly susceptible to motion.

Nonetheless, our study and the results achieved are limited by the included patient population and small sample size. Furthermore, even though in this work we used crossvalidation for reducing bias in classification, an independent validation dataset is required for generalizing the findings. Finally, in this work our research imaging protocol had to be adapted to the clinical setup constraints of our academic educational institution and, therefore, some of the imaging parameters may not be optimal; for example, in

quantitative imaging sequences, the voxel sizes are nonisotropic. Future works may benefit from optimization of parameter specifications for quantitative imaging sequences.

In conclusion, through investigation of a variety of conventional and quantitative MRI techniques applied on histopathologically proven tissue specimens, we demonstrated that incorporation of a few imaging techniques (comprising conventional MRI [T_2w and FLAIR] and DSC-MRI with DTI or IVIM) can form a multiparametric surrogate marker, predictive of tissue subregions prior to image-guided biopsy procedures.

Acknowledgments

Contract grant sponsor: Tehran University of Medical Sciences & Health Services; contract grant number: 28479; Tehran University of Medical Sciences and Health Services The authors thank Mohammad Peikari, PhD (Department of Medical Biophysics, University of Toronto, Canada) for sharing his code for analysis of histopathological data; Nima Gilani, PhD (Department of Cognitive Neuroscience, Maastricht University) for helping in analysis of IVIM/T_2-relaxometry data; and our MRI technician, Behrouz Rafiei, MSc (Imaging Center, Imam Hospital, Tehran University of Medical Sciences, Iran).

References

1. Claes A, Idema AJ, Wesseling P. Diffuse glioma growth: a guerilla war. Acta Neuropathol. 2007; 114:443–458. [PubMed: 17805551]
2. Louis DN, Perry A, Reifenberger G, et al. The 2016 World Health Organization classification of tumors of the central nervous system: a summary. Acta Neuropathol. 2016; 131:803–820. [PubMed: 27157931]
3. Boonzaier NR, Larkin TJ, Matys T, van der Hoorn A, Yan J-L, Price SJ. Multiparametric MR imaging of diffusion and perfusion in contrastenhancing and nonenhancing components in patients with glioblastoma. Radiology. 2017; 160150
4. Sottoriva A, Spiteri I, Piccirillo SG, et al. Intratumor heterogeneity in human glioblastoma reflects cancer evolutionary dynamics. Proc Natl Acad Sci USA. 2013; 110:4009–4014. [PubMed: 23412337]
5. Gatenby RA, Grove O, Gillies RJ. Quantitative imaging in cancer evolution and ecology. Radiology. 2013; 269:8–15. [PubMed: 24062559]
6. Marusyk A, Almendro V, Polyak K. Intra-tumour heterogeneity: a looking glass for cancer? Nat Rev Cancer. 2012; 12:323–334. [PubMed: 22513401]
7. Carlsson SK, Brothers SP, Wahlestedt C. Emerging treatment strategies for glioblastoma multiforme. EMBO Mol Med. 2014; 6:1359–1370. [PubMed: 25312641]
8. Chamberlain MC. Radiographic patterns of relapse in glioblastoma. J Neurooncol. 2011; 101:319–323. [PubMed: 21052776]
9. Delgado-Lopez PD, Corrales-Garcia EM. Survival in glioblastoma: a review on the impact of treatment modalities. Clin Transl Oncol. 2016; 18:1062–1071. [PubMed: 26960561]
10. Law M, Yang S, Wang H, et al. Glioma grading: sensitivity, specificity, and predictive values of perfusion MR imaging and proton MR spectroscopic imaging compared with conventional MR imaging. AJNR Am J Neuroradiol. 2003; 24:1989–1998. [PubMed: 14625221]
11. Watanabe M, Tanaka R, Takeda N. Magnetic resonance imaging and histopathology of cerebral gliomas. Neuroradiology. 1992; 34:463–469. [PubMed: 1436452]
12. Johnson PC, Hunt SJ, Drayer BP. Human cerebral gliomas: correlation of postmortem MR imaging and neuropathologic findings. Radiology. 1989; 170:211–217. [PubMed: 2535765]
13. Price SJ, Pena A, Burnet NG, et al. Tissue signature characterisation of diffusion tensor abnormalities in cerebral gliomas. Eur Radiol. 2004; 14:1909–1917. [PubMed: 15221264]
14. Nilsson M, van Westen D, Stahlberg F, Sundgren PC, Latt J. The role of tissue microstructure and water exchange in biophysical modelling of diffusion in white matter. MAGMA. 2013; 26:345–370. [PubMed: 23443883]

15. Le Bihan D, Lima M. Diffusion magnetic resonance imaging: what water tells us about biological tissues. PLoS Biol. 2015; 13:e1002203. [PubMed: 26204162]
16. Caseiras GB, Chheang S, Babb J, et al. Relative cerebral blood volume measurements of low-grade gliomas predict patient outcome in a multi-institution setting. Eur J Radiol. 2010; 73:215–220. [PubMed: 19201123]
17. Boxerman JL, Shiroishi MS, Ellingson BM, Pope WB. Dynamic susceptibility contrast MR imaging in glioma: review of current clinical practice. Magn Reson Imaging Clin N Am. 2016; 24:649–670. [PubMed: 27742108]
18. Hu LS, Eschbacher JM, Dueck AC, et al. Correlations between perfusion MR imaging cerebral blood volume, microvessel quantification, and clinical outcome using stereotactic analysis in recurrent high-grade glioma. AJNR Am J Neuroradiol. 2012; 33:69–76. [PubMed: 22095961]
19. Durst CR, Raghavan P, Shaffrey ME, et al. Multimodal MR imaging model to predict tumor infiltration in patients with gliomas. Neuroradiology. 2014; 56:107–115. [PubMed: 24337609]
20. Eidel O, Neumann JO, Burth S, et al. Automatic analysis of cellularity in glioblastoma and correlation with ADC using trajectory analysis and automatic nuclei counting. PLoS One. 2016; 11:e0160250. [PubMed: 27467557]
21. Leemans A, Jeurissen B, Sijbers J, Jones D. ExploreDTI: a graphical toolbox for processing, analyzing, and visualizing diffusion MR data. 17th Annual Meeting ISMRM; Honolulu. 2009. 3537
22. Wang W, Steward C, Desmond P. Diffusion tensor imaging in glioblastoma multiforme and brain metastases: the role of p, q, L, and fractional anisotropy. AJNR Am J Neuroradiol. 2009; 30:203–208. [PubMed: 18842762]
23. Fournet G, Li J-R, Cerjanic AM, Sutton BP, Ciobanu L, Le Bihan D. A two-pool model to describe the IVIM cerebral perfusion. J Cereb Blood Flow Metab. 2016 0271678X16681310.
24. Le Bihan D, Breton E, Lallemand D, Aubin M, Vignaud J, Laval-Jeantet M. Separation of diffusion and perfusion in intravoxel incoherent motion MR imaging. Radiology. 1988; 168:497–505. [PubMed: 3393671]
25. Gilani N, Malcolm P, Johnson G. A model describing diffusion in prostate cancer. Magn Reson Med. 2017; 78:316–326. [PubMed: 27439379]
26. Pavilla A, Gambarota G, Arrigo A, Mejdoubi M, Duvauferrier R, Saint-Jalmes H. Diffusional kurtosis imaging (DKI) incorporation into an intravoxel incoherent motion (IVIM) MR model to measure cerebral hypoperfusion induced by hyperventilation challenge in healthy subjects. MAGMA. 2017:1–10.
27. Peikari M, Martel AL. Automatic cell detection and segmentation from H and E stained pathology slides using colorspace decorrelation stretching. SPIE Med Imaging. 2016:979114–979116.
28. Holm S. A simple sequentially rejective multiple test procedure. Scand J Stat. 1979:65–70.
29. Akaike H. Selected Papers of Hirotugu Akaike. Berlin: Springer; 1998. Information theory and an extension of the maximum likelihood principle; 199–213.
30. Schwarz G. Estimating the dimension of a model. Ann Stat. 1978; 6:461–464.
31. Fathi Kazerooni A, Nabil M, Haghighat Khah H, et al. ADC-derived spatial features can accurately classify adnexal lesions. J Magn Reson Imaging. 2017 [Epub ahead of print].
32. Kazerooni AF, Malek M, Haghighatkhah H, et al. Semiquantitative dynamic contrast-enhanced MRI for accurate classification of complex adnexal masses. J Magn Reson Imaging. 2017; 45:418–427. [PubMed: 27367786]
33. Lope-Piedrafita S, Garcia-Martin ML, Galons JP, Gillies RJ, Trouard TP. Longitudinal diffusion tensor imaging in a rat brain glioma model. NMR Biomed. 2008; 21:799–808. [PubMed: 18470959]
34. Kim S, Pickup S, Hsu O, Poptani H. Diffusion tensor MRI in rat models of invasive and well-demarcated brain tumors. NMR Biomed. 2008; 21:208–216. [PubMed: 17530617]
35. Sternberg EJ, Lipton ML, Burns J. Utility of diffusion tensor imaging in evaluation of the peritumoral region in patients with primary and metastatic brain tumors. AJNR Am J Neuroradiol. 2014; 35:439–444. [PubMed: 24052506]
36. Macyszyn L, Akbari H, Pisapia JM, et al. Imaging patterns predict patient survival and molecular subtype in glioblastoma via machine learning techniques. Neurooncology. 2016; 18:417–425.

37. Sadeghi N, D'Haene N, Decaestecker C, et al. Apparent diffusion coefficient and cerebral blood volume in brain gliomas: relation to tumor cell density and tumor microvessel density based on stereotactic biopsies. AJNR Am J Neuroradiol. 2008; 29:476–82. [PubMed: 18079184]

38. Barajas RF Jr, Phillips JJ, Parvataneni R, et al. Regional variation in histopathologic features of tumor specimens from treatment-naive glioblastoma correlates with anatomic and physiologic MR imaging. Neurooncology. 2012; 14:942–954.

39. Hu LS, Ning S, Eschbacher JM, et al. Multi-parametric MRI and texture analysis to visualize spatial histologic heterogeneity and tumor extent in glioblastoma. PLoS One. 2015; 10:e0141506. [PubMed: 26599106]

40. Kazerooni AF, Mohseni M, Rezaei S, Bakhshandehpour G, Rad HS. Multi-parametric (ADC/PWI/T2-w) image fusion approach for accurate semi-automatic segmentation of tumorous regions in glioblastoma multiforme. MAGMA. 2015; 28:13–22. [PubMed: 24691860]

41. Ion-Margineanu A, Van Cauter S, Sima DM, et al. Classifying glioblastoma multiforme follow-up progressive vs. responsive forms using multi-parametric MRI features. Front Neurosci. 2017; 10:615. [PubMed: 28123355]

42. Emblem KE, Nedregaard B, Hald JK, Nome T, Due-Tonnessen P, Bjornerud A. Automatic glioma characterization from dynamic susceptibility contrast imaging: Brain tumor segmentation using knowledge-based fuzzy clustering. J Magn Reson Imaging. 2009; 30:1–10. [PubMed: 19557840]

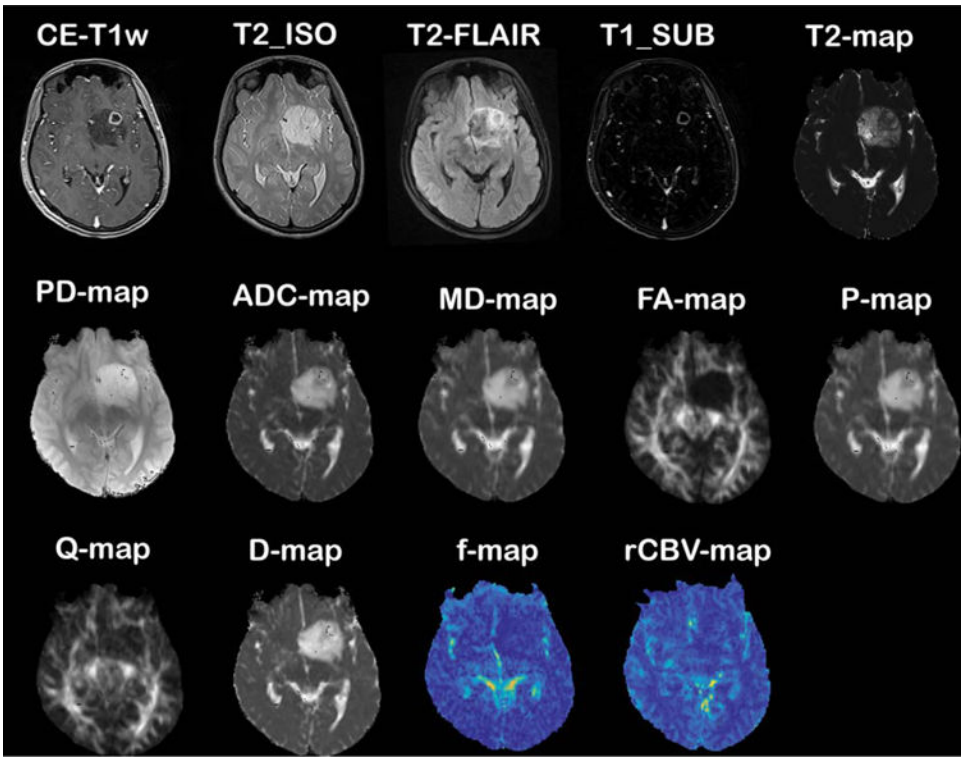

FIGURE 1.

MR images and quantitative maps of a 20-year-old female with histopathologically confirmed grade II oligodendroglioma (images are coregistered with CE-T_1w image).

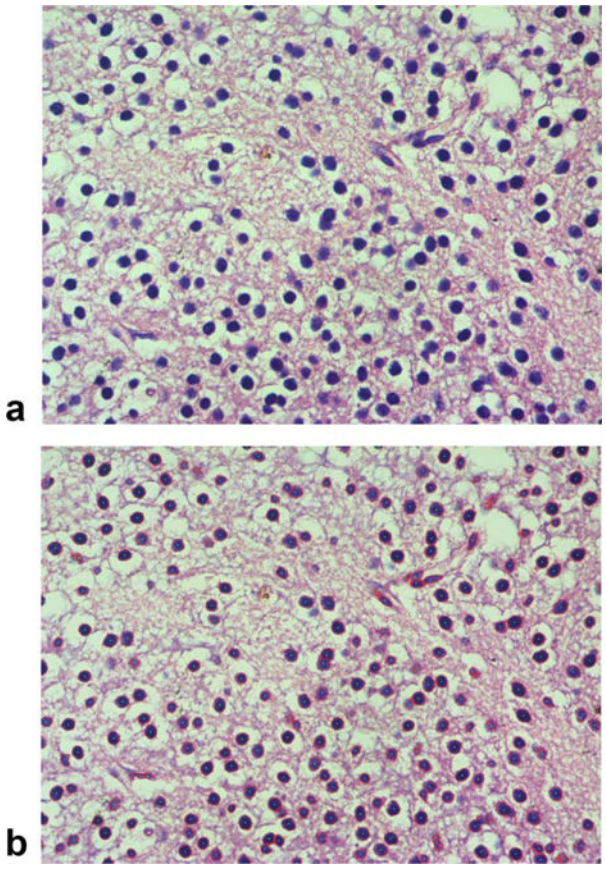

FIGURE 2.

Automated segmentation of cells in microscopic images (×40 magnification): (**A**) sample image from tumor core of the same patient indicated in Fig. 1; (**B**) automated cell segmentation result.

TABLE 1

MRI Specifications

Sequence	TE/TR	Slice thickness (mm)	Flip angle	FOV (mm^2)	Image matrix	Other specifications
Pre- and postcontrast 3D T1w	5/17	1	25°	208 × 256	208 × 256	N/A
3D T2w	200/2500	1	120°	208 × 256	420 × 512	N/A
T2-FLAIR	115/8400	5	125°	181 × 200	232 × 256	TI = 2240
T2-Relaxometry	(12, 24, 36, 48, 60, 72, 84, 96, 108, 120, 132, 144, 156, 168, 180, 192)/ 4000	5	180°	200 × 200	232 × 256	N/A
DWI	100/4000	5	90°	200 × 200	136 × 136	b-values = 50, 1000 s/mm^2
Multi b-value DWI	100/4000	5	90°	200 × 200	136 × 136	b-values = 0, 50, 200, 400, 600, 800, 1000 s/mm^2
DTI	90/9000	5	90°	256 × 256	128 × 128	b-values = 50, 1000 s/mm^2
DSC-MRI	30/1600	5	70°	220 × 220	128 × 128	No. Dynamic Scans = 64, Temporal Resolution = 1.5 s

DWI: Diffusion Weighted Imaging; DTI: Diffusion Tensor Imaging; DSC-MRI: Dynamic Susceptibility Contrast Enhanced MRI.

TABLE 2

Correlations (in Terms of *R*) Among the MRI-Derived Parameters With Each Other and Between MRI-Derived Parameters and Cell Count (From Histopathology)[a]

	ADC	CBV	D	D*	FA	FLAIR	f	K	MD	P	PD	Q	T1_SUB	T2_ISO	T2	Count
ADC		−0.078	**0.96**	−0.40	**−0.60**	0.45	−0.11	**−0.71**	**0.91**	**0.88**	0.28	−0.28	0.13	**0.66**	**0.80**	0.30
CBV			0.01	0.14	−0.25	0.03	**0.35**	0.17	−0.09	−0.06	0.18	−0.24	0.28	−0.22	−0.19	**0.46**
D				−0.31	**−0.64**	0.46	−0.09	**−0.68**	**0.90**	**0.88**	0.26	−0.31	0.15	**0.64**	**0.78**	**0.40**
D*					0.30	−0.25	0.15	0.43	−0.38	−0.40	−0.25	0.30	−0.09	−0.30	**−0.49**	−0.02
FA						−0.33	0.10	0.58	**−0.56**	**−0.58**	−0.41	**0.86**	−0.20	−0.39	**−0.54**	**−0.37**
FLAIR							0.14	−0.43	0.41	0.44	0.21	−0.14	0.37	**0.69**	0.34	0.05
f								**0.36**	0.01	−0.01	0.07	0.08	0.27	0.10	−0.07	0.32
K									**−0.60**	**−0.59**	−0.18	0.41	−0.19	−0.51	**−0.61**	−0.09
MD										**0.98**	0.46	−0.28	0.19	**0.62**	**0.84**	**0.36**
P											0.47	−0.31	0.26	**0.59**	**0.81**	**0.36**
PD												−0.47	0.27	0.02	0.39	0.00
Q													−0.23	−0.11	−0.34	−0.17
T1_SUB														0.03	0.03	0.23
T2_ISO															**0.69**	0.15
T2																0.18

[a]The cells with bold-face type and with gray-shaded color are those with significant correlation as indicated by Spearman's rank correlation.

ADC: Apparent Diffusion Coefficient (DWI); CBV: Cerebral Blood Volume (DSC-MRI); D: True diffusion coefficient (IVIM);

D*: Pseudo-diffusion coefficient (IVIM); f: perfusion fraction (IVIM); K: Diffusion Kurtosis; MD: Mean Diffusivity (DTI); FA: Fractional Anisotropy (FA); P: Pure isotropic diffusion coefficient (DTI); Q: Pure anisotropic diffusion coefficient (DTI); PD: Proton Density (T2-relaxometry); T_2: T2 relaxation time (T2-relaxometry); T1_SUB: Subtracted high-resolution T1w from the corresponding high-resolution contrast-enhanced T1w image; T2_ISO: High-resolution T2w image; FLAIR: Fluid-attenuated inversion recovery image.

TABLE 3

Comparison of the Mean Values Based on ANOVA Test (Second Column), for Differentiation of Normal Tissue (NT) vs. Infiltrative Edema (IE) vs. Active Tumor (AT) Simultaneously, and Evaluating the Diagnostic Performances of Individual Parameters in Differentiating Pairwise Regions, ie, "NT" from "IE," "NT" from "AT," and "IE" from "AT" Using Cross-validated LDA Method[a]

Feature	ANOVA Test (*P*-values)	NT from IE					NT from AT					IE from AT				
		***P*-values**	**Sens.**	**Spec.**	**Acc.**	**AUC (95% CI)**	***P*-values**	**Sens.**	**Spec.**	**Acc.**	**AUC (95% CI)**	***P*-values**	**Sens.**	**Spec.**	**Acc.**	**AUC (95% CI)**
T1_SUB	0.203	0.563	100	0	71.4	68.8 (45.0–92.5)	0.176	50	100	78.6	**81.2** (54.1–100)	0.462	1.9	95.1	73.7	67.5 (36.4–98.1)
T2_ISO	**0.001**	**0.018**	87.0	75.9	83.9	**89.4** (77.0–100)	**0.000**	77.9	87.5	83.5	**95.8** (86.0–100)	0.913	0.0	100	76.9	59.1 (35.5–82.8)
FLAIR	**0.001**	**0.016**	89.8	64.7	82.7	**90.6** (79.0–100)	**0.000**	67.9	87.5	79.1	**93.7** (81.2–100)	0.958	0.0	100	76.9	49.2 (21.8–76.5)
ADC	**0.005**	**0.002**	89.6	87.5	89.0	**90.0** (76.9–100)	**0.001**	100	87.5	92.9	**100** (100–100)	0.473	0.64	100	77.1	65.0 (41.9–88.1)
CBV	**0.004**	0.963	100	0	71.4	50.7 (24.1–77.3)	**0.003**	66.7	87.5	78.6	**75.0** (41.1–100)	**0.018**	51.3	95.4	85.2	**80.0** (50.7–100)
MD	**0.000**	**0.001**	93.9	63.8	85.3	**93.8** (85.0–100)	**0.001**	100	100	100	**100** (100–100)	0.601	1.3	100	77.2	68.3 (46.3–90.3)
FA	**0.010**	0.082	94.6	12.9	71.3	70.6 (50.2–91.0)	**0.007**	100	85.5	91.8	**100** (100–100)	0.209	0.0	100	76.9	86.7 (71.0–100)
Q	0.116	0.215	100	0	71.4	51.9 (27.5–76.4)	0.104	77.6	80.4	79.7	83.3 (58.6–100)	0.990	5.8	98.6	77.2	82.5 (65.4–99.3)
P	**0.000**	**0.001**	89.7	69.2	84.0	**91.9** (81.0–100)	**0.002**	100	99.1	99.5	**100** (100–100)	0.737	0.0	100	76.9	60.0 (35.3–84.7)
D	**0.000**	**0.002**	90.0	71.4	84.9	**90.6** (78.6–100)	**0.000**	100	94.0	96.7	**100** (100–100)	0.251	9.9	99.0	78.5	68.3 (46.0–90.6)
D*	0.748	0.918	98.9	0.9	70.9	60.6 (31.8–89.5)	0.734	41.2	74.1	61.5	60.4 (24.4–95.9)	0.855	0.0	100	76.9	52.2 (23.5–80.8)
f	0.505	0.941	100	0	71.4	52.0 (27.1–76.8)	0.504	32.6	86.1	63.7	59.5 (27.8–90.7)	0.574	0.6	97.6	75.2	64.2 (39.9–88.4)
K	0.1136	0.906	93.5	14.9	71.2	73.7 (52.9–94.6)	0.165	83.3	86.5	85.2	**87.5** (65.8–100)	0.145	0	100	76.9	55.8 (32.4–79.3)
T_2	**0.018**	**0.024**	93.3	66.8	86.0	**84.4** (65.4–100)	**0.041**	83.3	87.5	85.7	**87.5** (67.8–100)	0.890	0.0	100	76.9	50.1 (24.4–75.8)
PD	0.282	0.461	100	0.51	71.6	66.9 (43.0–90.7)	0.272	42.9	86.5	68.1	72.9 (42.7–100)	0.738	2.1	100	77.4	55.1 (23.4–86.9)
Count	**8.9E-06**	0.221	92.5	25.9	73.5	**83.8** (68.5–98.9)	**1.0E-05**	66.7	100	85.7	**100** (100–100)	**6.1E-05**	66.7	99.8	92.1	91.7 (79.2–100)

[a]The values with bold-face type under the *P*-values columns belong to parameters with significant *P*-values: the column labeled as "ANOVA Test" shows *P*-values obtained based on the ANOVA test for simultaneous differentiation of the three regions from each other; the other three columns under the parts "NT from IE," "NT from AT," and "IE from AT" parts, labeled as "P-values," indicate P-values calculated for pairwise differentiation of the regions based on Tukey-HSD or Games-Howell tests (whichever was appropriate for each parameter). The bold-face type values under other columns indicate high accuracy

TABLE 4

Evaluating Accuracy and Diagnostic Performances (AUC) of LDA, QDA, and SVM Classifiers on the Selected Features[a]

Feature selection method	Selected features	Accuracy (%)	AUC (95% CI) (%)
Cross-Validated LDA			
Backward AIC	CBV, FLAIR, MD, T2_ISO	**82.8**	**89.3** (75.9-100)
Backward BIC	CBV, MD	75.4	74.7 (55.0-94.4)
Forward/Stepwise AIC	CBV, D, T2_ISO	**82.1**	**91.9** (83.1-100)
Backward BIC	CBV, D	74.8	73.2 (54.4-91.6)
Cross-Validated QDA			
Backward AIC	CBV, FLAIR, MD, T2_ISO	**85.1**	**92.4** (84.1-100)
Backward BIC	CBV, MD	79.9	80.0 (61.8-98.0)
Forward/Stepwise AIC	CBV, D, T2_ISO	83.4	85.3 (71.2-99.1)
Backward BIC	CBV, D	81.2	84.8 (69.1-99.4)
Cross-Validated SVM			
Backward AIC	CBV, FLAIR, MD, T2_ISO	**91.3**	**91.9** (79.6-100)
Backward BIC	CBV, MD	80.2	79.8 (61.4-98.1)
Forward/Stepwise AIC	CBV, D, T2_ISO	79.3	83.0 (65.9-99.7)
Backward BIC	CBV, D	79.3	81.4 (63.6-98.8)

[a]The gray-shaded cells with bold-type face numbers or letters indicate highest diagnostic performances.

TABLE 5

Evaluating Classification Performances of LDA, QDA, and SVM Classifiers on the Selected Features for Differentiation of Each of Two Tissue Subregions From Each Other, ie, NT From IE, NT From AT, and IE From AT[a]

Classifiers	Feature combinations	NT from IE				NT from AT				IE from AT			
		Sens.	Spec.	Acc.	AUC (95% CI)	Sens.	Spec.	Acc.	AUC (95% CI)	Sens.	Spec.	Acc.	AUC (95% CI)
LDA	CBV, FLAIR, MD, T2_ISO	90.0	86.8	89.1	94.8 (86.4–100)	100	100	100	100 (100–100)	57.9	99.8	90.1	92.0 (80.0–100)
	CBV, MD	91.1	65.9	84.0	92.6 (83.1–100)	100	100	100	100 (100–100)	62.3	99.6	91.1	91.5 (79.0–100)
	CBV, D, T2_ISO	86.1	94.1	88.5	91.7 (80.5–100)	100	100	100	100 (100–100)	50.6	100	88.6	91.4 (78.6–100)
	CBV, D	89.6	64.2	82.5	90.0 (77.7–100)	100	100	100	100 (100–100)	50.6	100	88.6	91.3 (78.3–100)
QDA	CBV, FLAIR, MD, T2_ISO	**85.2**	**99.5**	**89.3**	**92.3 (83.9–99.9)**	**100**	**100**	**100**	**100 (100–100)**	**84.1**	**94.4**	**92.0**	**89.2 (72.5–100)**
	CBV, MD	86.6	73.4	82.9	80.0 (61.6–98.0)	100	100	100	100 (100–100)	66.7	99.6	92.0	83.1 (83.1–100)
	CBV, D, T2_ISO	**81.4**	**89.8**	**93.9**	**85.6 (71.7–99.0)**	**100**	**100**	**100**	**100 (100–100)**	**83.3**	**99.8**	**96.0**	**91.6 (91.6–100)**
	CBV, D	85.5	83.4	85.1	84.5 (68.6–99.3)	100	100	100	100 (100–100)	61.1	100	91.1	80.6 (59.1–98.9)
SVM	CBV, FLAIR, MD, T2_ISO	**94.6**	**89.8**	**93.3**	**98.8 (95.9–100)**	**100**	**100**	**100**	**100 (100–100)**	**85.4**	**100**	**96.6**	**100 (100–100)**
	CBV, MD	93.7	65.2	85.6	94.6 (86.8–100)	100	100	100	100 (100–100)	69.5	100	92.9	93.5 (80.2–100)
	CBV, D, T2_ISO	88.3	86.9	88.0	92.9 (82.9–100)	100	100	100	100 (100–100)	50.6	100	88.6	91.1 (77.8–100)
	CBV, D	91.1	61.4	82.7	91.4 (79.8–100)	100	100	100	100 (100–100)	50.6	100	88.6	91.6 (78.7–100)

[a]The gray-shaded cells with bold-type face numbers or letters indicate highest diagnostic performances of classifiers for all three discrimination.